nature ecology & evolution

SUPPLEMENTARY INFORMATION

DOI: 10.1038/s41559-017-0277-5

In the format provided by the authors and unedited.

Ecosystem functioning is enveloped by hydrometeorological variability

Christoforos Pappas[1]*, Miguel D. Mahecha[2,3], David C. Frank[4,5], Flurin Babst[4,6] and Demetris Koutsoyiannis[7]

[1]Département de Géographie and Centre d'Études Nordiques, Université de Montréal, Montréal, QC H2V 2B8, Canada. [2]Max Planck Institute for Biogeochemistry, 07745 Jena, Germany. [3]German Centre for Integrative Biodiversity Research (iDiv) Halle-Jena-Leipzig, 04103 Leipzig, Germany. [4]Swiss Federal Research Institute, WSL, 8903 Birmensdorf, Switzerland. [5]Laboratory of Tree-Ring Research, University of Arizona, Tucson, Arizona 85721-0045, USA. [6]W. Szafer Institute of Botany, Polish Academy of Sciences, 31-512 Krakow, Poland. [7]Department of Water Resources and Environmental Engineering, School of Civil Engineering, National Technical University of Athens, 15780 Athens, Greece. *e-mail: christoforos.pappas@umontreal.ca

Supporting information for:

Ecosystem functioning is enveloped by hydrometeorological variability

Christoforos Pappas[1*], Miguel D. Mahecha[2,3], David C. Frank[4,5], Flurin Babst[4,6], and Demetris Koutsoyiannis[7]

[1] Département de géographie and Centre d'études nordiques, Université de Montréal, Montréal, QC, Canada

[2] Max Planck Institute for Biogeochemistry, 07745 Jena, Germany

[3] German Centre for Integrative Biodiversity Research (iDiv) Halle-Jena-Leipzig, Leipzig, Germany

[4] Swiss Federal Research Institute, WSL, Birmensdorf, Switzerland

[5] Laboratory of Tree-Ring Research, University of Arizona, USA

[6] W. Szafer Institute of Botany, Polish Academy of Sciences, Krakow, Poland

[7] Department of Water Resources and Environmental Engineering, School of Civil Engineering, National Technical University of Athens, Greece

This file provides supporting information for:

1. the analysed datasets, including (a) hydrometeorological and (b) ecosystem variables, as well as (c) simulation results with process-based ecosystem models (TRENDY model output);

2. the estimation of the composite continuum of hydrometeorological and ecosystem variability based on several datasets (empirical climacograms);

3. the fitting procedure of theoretical and empirical climacograms used to describe the continuum of hydrometeorological and ecosystem variability;

4. the analytical derivation of standard deviation as a function of averaging time scale for a single harmonic function.

[*] Corresponding author: Christoforos Pappas, Département de géographie, Université de Montréal, 520 ch. de la Côte Sainte-Catherine, Montréal, QC, H2V 2B8, CA (christoforos.pappas@umontreal.ca)

S1 Detailed data description

The analysed datasets, used as proxies for ecosystem functioning, and the resulting ecosystem variability, are summarized in Table S1, while the datasets used for the hydrometeorological variability are reported in Table S2.

S1.1 Micrometeorological and eddy covariance data

Micrometeorological and eddy covariance flux measurements [e.g., *Baldocchi*, 2003, 2008, 2014] from the FLUXNET2015 dataset (December 2015 release) are used (http://fluxnet.fluxdata.org/data/fluxnet2015-dataset/fullset-data-product/). This dataset consists of half-hourly data (level 4) of precipitation, air temperature, incoming shortwave radiation, vapour pressure deficit (VPD), and net ecosystem exchange (NEE), which are averaged to hourly time step.

Table S1. Datasets used for the analysis of ecosystem variability across time scales.

Measurement type	Variable	Temporal resolution [1]	Source
Eddy covariance flux	Net Ecosystem Exchange (NEE)	hourly	FLUXNET2015 [2]
Remote sensing	FAPAR	monthly	MODIS TIP [3], GIMMS
	LAI	monthly	MODIS TIP [3], GIMMS
Dendrochronological	Tree ring width	annual	Babst et al., 2014a,b
	Above-ground woody biomass	annual	Babst et al., 2014a,b

[1] It refers to the temporal resolution used in the analysis and not necessarily to the original temporal resolution of each dataset.
[2] One site with long-term measurements from the LaThuile Dataset that was not included in the FLUXNET2015 dataset (December 2015 release) is also incorporated in the analysis (see Table S3).
[3] Pinty et al., 2011
[4] Zhu et al., 2013

S1.1.1 Sensitivity to the pre-processing method of NEE

Estimates of NEE based on different pre-processing procedure (Ustar thresholds, where Ustar is the surface friction velocity threshold used for assessing the mixing condition of the air), as provided by the FLUXNET2015 dataset, are analysed[†]. This allows us to quantify the sensitivity of the $\log \sigma_{NEE} - \log k$ relation, where σ_{NEE} is the standard deviation of NEE at different averaging scales k, to different NEE products. Figure S1 illustrates the results for five European sites (similar is the case also for the other sites; results not shown). The following variables are used (detailed documentation is provided in the FLUXNET2015 dataset): NEE_[UT]_REF: reference NEE estimated with the model efficiency approach using method UT (Constant Ustar Threshold, CUT or Variable Ustar Threshold, VUT). NEE_[UT]_USTAR50: NEE estimated using method UT (CUT, VUT) for each year from 50 percentile of USTAR threshold. NEE_[UT]_MEAN: NEE estimated using method UT (CUT, VUT) across years, average from 40 NEE_[UT]_50 versions,

[†] Note that for the site FR-LBr (Table S3) that is not included in the FLUXNET2015 dataset (December 2015 release), the variables provided by the LaThuile2007 dataset are used, namely: Ta_f, VPD_f, Precip, Rg_f, NEE_st_fANN.

where NEE_[UT]_50 is the 50-percentile of the NEE estimates. The analysed estimates of NEE lead to very similar $\log_{10} \sigma_{NEE} - \log_{10} k$ patterns, thus supporting the robustness of our findings.

Table S2. Climatic datasets used to describe the hydrometeorological envelope of variability across time scales.

Dataset	Variable	Temporal resolution	Source
Micrometeorological	Air temperature	1 h	http://fluxnet.fluxdata.org/2015/12/31/fluxnet2015-dataset-release/
	Precipitation	1 h	
	Shortwave radiation (incoming)	1 h	
	Vapour pressure deficit	1 h	
CRU-NCEPv4	Air temperature	6 h	http://dods.extra.cea.fr/data/p529viov/cruncep/
	Precipitation	6 h	
	Shortwave radiation (incoming)	6 h	
	Vapour pressure deficit [1]	6 h	
ERA Interim	Air temperature	1 d	http://apps.ecmwf.int/datasets/data/interim-full-daily
	Precipitation	1 d	
	Shortwave radiation (incoming)	1 d	
	Vapour pressure deficit [1]	1 d	
NCEP I, II	Air temperature	6 h	http://www.esrl.noaa.gov/psd/data/gridded/reanalysis/
	Precipitation	6 h	
	Shortwave radiation (incoming)	6 h	
	Vapour pressure deficit [1]	6 h	
20th Century Reanalysis Version v2c	Air temperature	3 h	http://www.esrl.noaa.gov/psd/data/20thC_Rean/
	Precipitation	3 h	
	Shortwave radiation (incoming)	3 h	
	Vapour pressure deficit [1]	3 h	
CRU TS 1.2	Air temperature	1 mon	https://crudata.uea.ac.uk/cru/data/hrg/timm/grid/CRU_TS_1_2.html
	Precipitation	1 mon	
	Vapour pressure deficit [1]	1 mon	
CRU TS 3.23	Air temperature	1 mon	https://crudata.uea.ac.uk/cru/data/hrg/cru_ts_3.23/
	Precipitation	1 mon	
	Vapour pressure deficit [1]	1 mon	

[1] Calculated with the Clausius-Clapeyron equation.

S1.1.2 Sensitivity to data-gaps and gap-filling method

For the case of micrometeorological variables, the sensitivity of the $\log \sigma - \log k$ relation to data gaps is assessed by examining different gap-filling approaches. Figure S2 illustrates the results for five European eddy covariance flux towers when different gap-filling methods, available from the FLUXNET2015 dataset, are applied. The results are very similar for all the examined locations (results not shown). The following variables are used (for more details see the complete documentation of the FLUXNET2015 dataset): TA_F_MDS: air temperature, gap-filled using Marginal Distribution Sampling (MDS) method; TA_ERA: air temperature, downscaled from ERA, linearly regressed using measured only site data; TA_F: air temperature, consolidated from TA_F_MDS and TA_ERA. SW_IN_F_MDS: shortwave radiation, incoming, gap-filled using

MDS; SW_IN_ERA: shortwave radiation, incoming, downscaled from ERA, linearly regressed using measured only site data; SW_IN_F: shortwave radiation, incoming consolidated from SW_IN_F_MDS and SW_IN_ERA. VPD_F_MDS: vapour pressure deficit, gap-filled using MDS; VPD_ERA: vapour pressure deficit, downscaled from ERA, linearly regressed using measured only site data; VPD_F: vapour pressure deficit consolidated from VPD_F_MDS and VPD_ERA. P: precipitation; P_ERA: precipitation, downscaled from ERA, linearly regressed using measured only site data; P_F: precipitation consolidated from P and P_ERA. Different gap-filled data lead to fairly similar patterns of confirming the robustness of our findings.

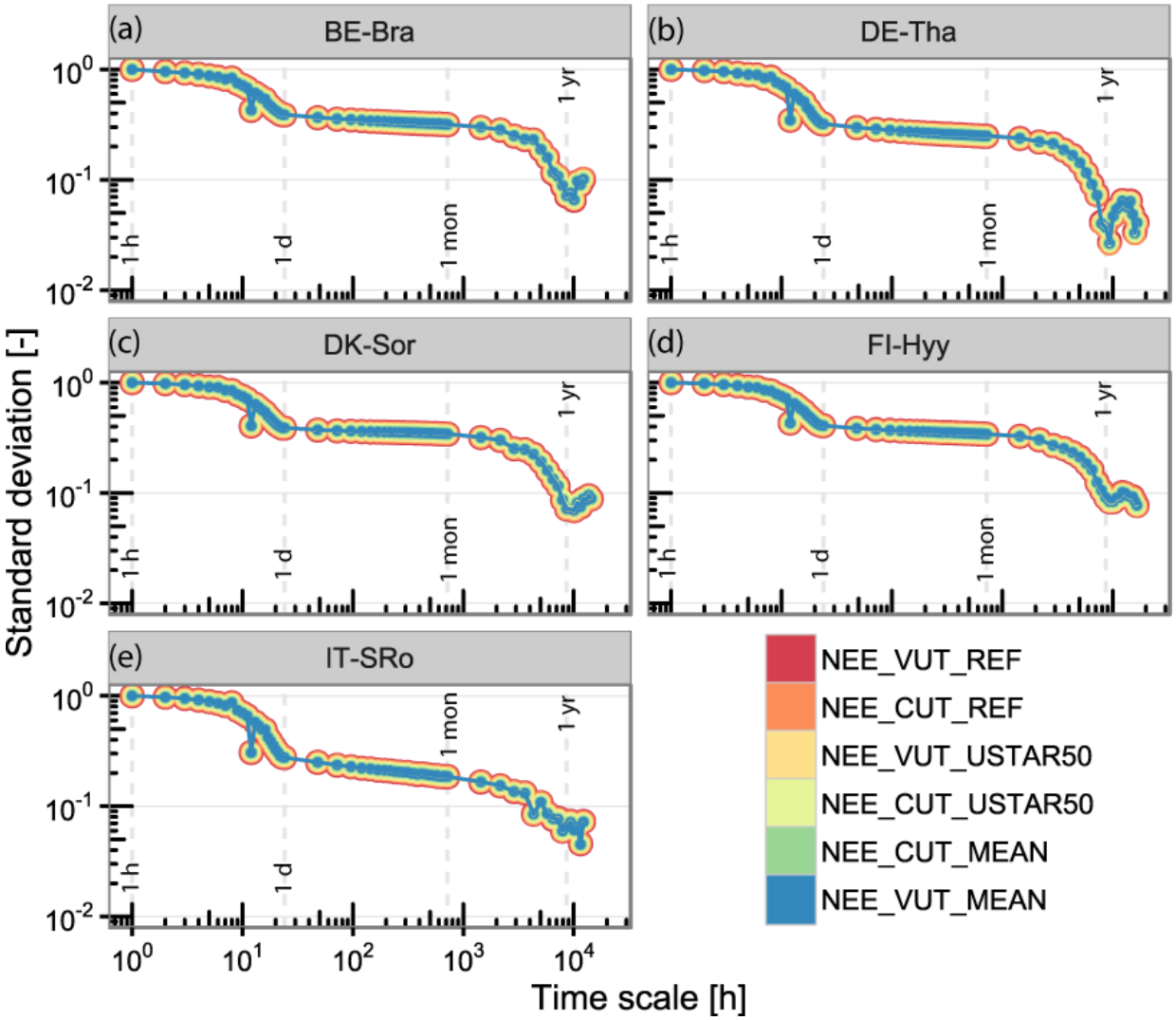

Figure S1. Standard deviation of Net Ecosystem Exchange (σ_{NEE}) as a function of the averaging time scale, k, for five European sites (subplots a-e; see Table S3). Different colours and point sizes correspond to NEE estimates based on six different pre-processing methods (see supporting text). For the sake of clarity, for averaging scales from one hour to one day, one day to one month, and larger than one month, hourly, daily, and monthly averaging time steps are used, respectively. All six pre-processing methods lead to very similar estimates of the $\log \sigma_{NEE} - \log k$ relation.

Table S3. Site description of the 23 analysed micrometeorological and eddy covariance flux tower data. [1]DBF: Deciduous Broadleaf Forest; EBF: Evergreen Broadleaf Forest; ENF: Evergreen Needleleaf Forest; MF: Mixed Forest. [2]Sites where tree-ring and above ground woody biomass estimates are available. [3]Data from the La Thuile 2007 database, while the data from all the other sites are from the FLUXNET2015 release. [*]Data-gap in 2003. [**]Data-gap in 1998. [&]Data-gap in 2009. [&&]Data-gap in 2009, 2010, and 2011. [#]Data-gap in 2007, 2008, and 2009. [##]Data-gap in 1999.

Site ID	Longitude [deg]	Latitude [deg]	Elevation [m a.s.l.]	Length [yr]	From [yr]	To [yr]	Vegetation type[1]	Site name	Reference
AU-Tum	-35.66	148.15	932	13	2001	2013	EBF	Tumbarumba	Leuning *et al.,* 2005
BE-Bra[2]	51.31	4.52	16	17[*]	1996	2013	MF	Brasschaat (De Inslag Forest)	Carrara *et al.,* 2003
BE-Vie	50.31	6.00	493	19	1996	2014	MF	Vielsalm	Aubinet *et al.,* 2002
CA-Gro	48.22	-82.16	340	12	2003	2014	MF	Ontario - Groundhog River Boreal Mixedwood Forest	McCaughey *et al.,* 2006
CZ-BK1	49.50	18.54	908	13	2000	2012	ENF	Bily Kriz - Beskidy Mountains	Marek *et al.,* 2011
DE-Hai	51.08	10.45	430	13	2000	2012	DBF	Hainich	Knohl *et al.,* 2003
DE-Tha[2]	50.96	13.57	380	19	1996	2014	ENF	Anchor Station Tharandt	Grünwald and Bernhofer 2007
DK-Sor[2]	55.49	11.64	40	17	1996	2012	DBF	Soroe - LilleBogeskov	Pilegaard *et al.,* 2011
FI-Hyy[2]	61.85	24.30	181	19	1996	2014	ENF	Hyytiala	Suni *et al.,* 2003
FR-Pue	43.74	3.60	270	14	2000	2013	EBF	Puechabon	Allard *et al.,* 2008
IT-Lav	45.96	11.28	1353	10	2003	2012	ENF	Lavarone	Marcolla *et al.,* 2003
IT-Ren	46.59	11.43	1730	15[**]	1998	2013	ENF	Renon/Ritten (Bolzano)	Montagnani *et al.,* 2009
IT-Ro2	42.39	11.92	160	10[&]	2002	2012	DBF	Roccarespampani 2	Tedeschi *et al.,* 2006
IT-SRo[2]	43.73	10.28	6	14	1999	2012	ENF	San Rossore	Chiesi *et al.,* 2005
NL-Loo	52.17	5.74	25	19	1996	2014	ENF	Loobos	Dolman *et al.,* 2002
RU-Fyo	56.46	32.92	265	16	1998	2013	ENF	Fyodorovskoye wet spruce stand	https://fluxnet.ornl.gov/site/709
US-Blo	38.90	-120.63	1315	11	1997	2007	ENF	Blodgett Forest	Goldstein *et al.,* 2000
US-Ha1	42.54	-72.17	340	22	1991	2012	DBF	Harvard Forest EMS Tower	Urbanski *et al.,* 2007
US-MMS	39.32	-86.41	275	16	1999	2014	DBF	Morgan Monroe State Forest	Schmid *et al.,* 2000
US-Oho	41.55	-83.84	230	10	2004	2013	DBF	Oak Openings	DeForest *et al.,* 2006
US-Syv	46.24	-89.35	540	11[&&]	2001	2014	MF	Sylvania Wilderness Area	Desai *et al.,* 2005
US-WCr	45.81	-90.08	520	13[#]	1999	2014	DBF	Willow Creek	Cook *et al.,* 2004
FR-LBr[3]	44.72	-0.77	61	12[##]	1996	2008	ENF	Le Bray	Berbigier *et al.,* 2001

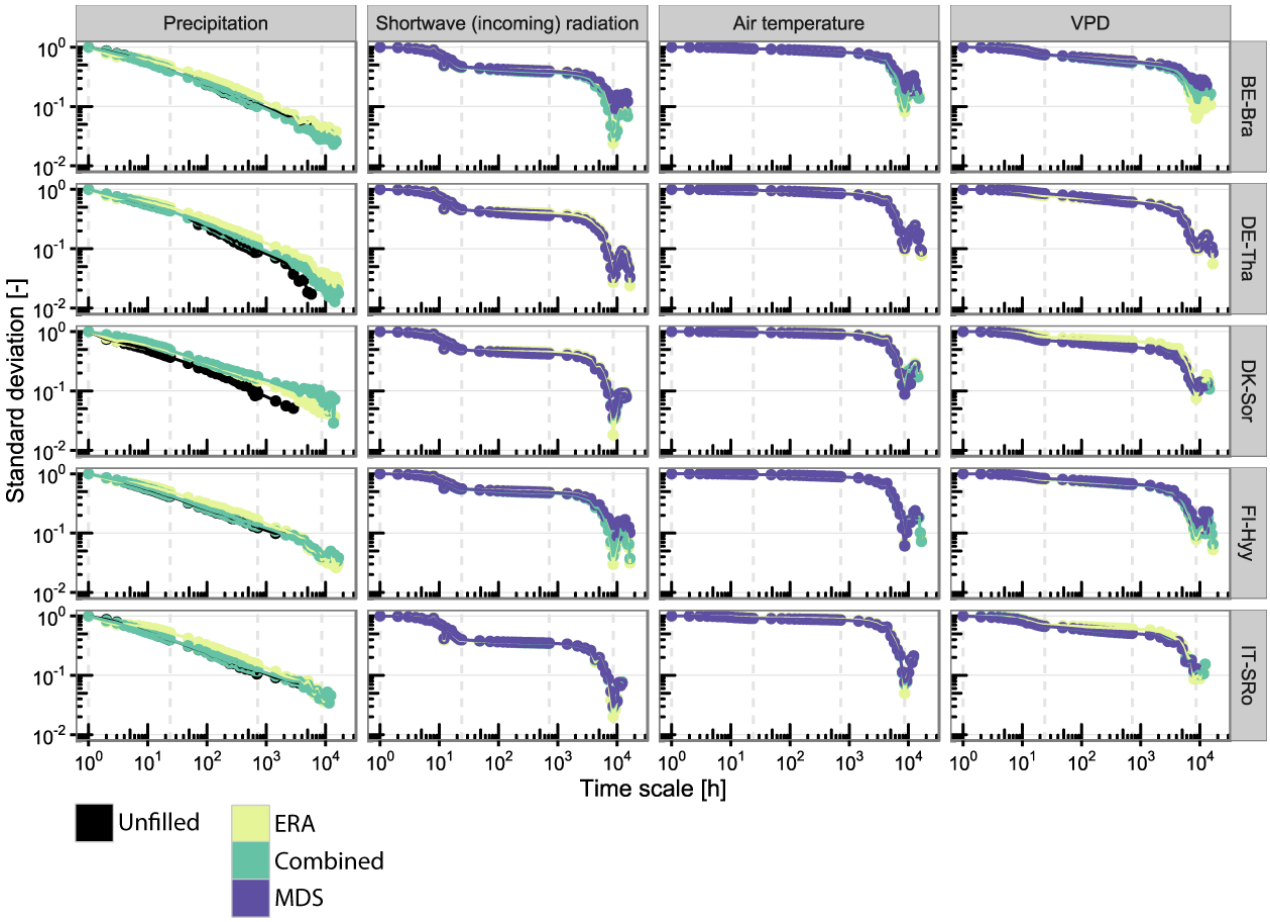

Figure S2. Standard deviation (σ) of the analysed hydrometeorological variables (columns) as a function of the averaging time scale, k, for five European sites (rows; see Table S3). Different colours correspond to products with different gap-filling methods. MDS stands for Marginal Distribution Sampling [*Moffat et al.*, 2007], ERA corresponds to values downscaled from the ERA reanalysis product, while 'Combined' refers to the final gap-filled product consolidated from MDS and ERA estimates. For the sake of figure's clarity, for averaging scales from one hour to one day, one day to one month, and larger than one month, hourly, daily, and monthly averaging time steps are used, respectively. Differently gap-filled data lead to fairly similar estimates of the $\log \sigma - \log k$ relation.

S1.1.3 Variability continua of eddy-covariance-derived GPP and RECO

Together with NEE, the variability of other ecosystem variables, related to the terrestrial carbon cycle is also analysed. More specifically, eddy covariance measurements of NEE can be partitioned to Gross Primary Productivity (GPP) and ecosystem respiration (RECO) using various assumptions and numerical algorithms [e.g., *Reichstein et al.*, 2005]. The variability continua of NEE, GPP, and RECO are presented in Figure S3. For the sites included in the FLUXNET2015 dataset the following variables are used: NEE_VUT_MEAN, GPP_NT_VUT_MEAN, RECO_NT_VUT_MEAN, while for the site from the la Thuile dataset NEE_st_fANN, GPP_st_ANN, and Reco_st are used.

However, for the composite ecosystem variability continuum, we use NEE data since this variable is a direct measurement rather than a modelling result (cf. GPP, RECO) and is close related to the additional proxy variables used for extrapolating the ecosystem variability continuum at longer

time scales. Partitioning the different components of the observed ecosystem carbon fluxes (GPP, RECO) introduces additional assumptions and uncertainties [e.g., *Wehr et al.*, 2016]. Thus within the frame of our analysis NEE is selected.

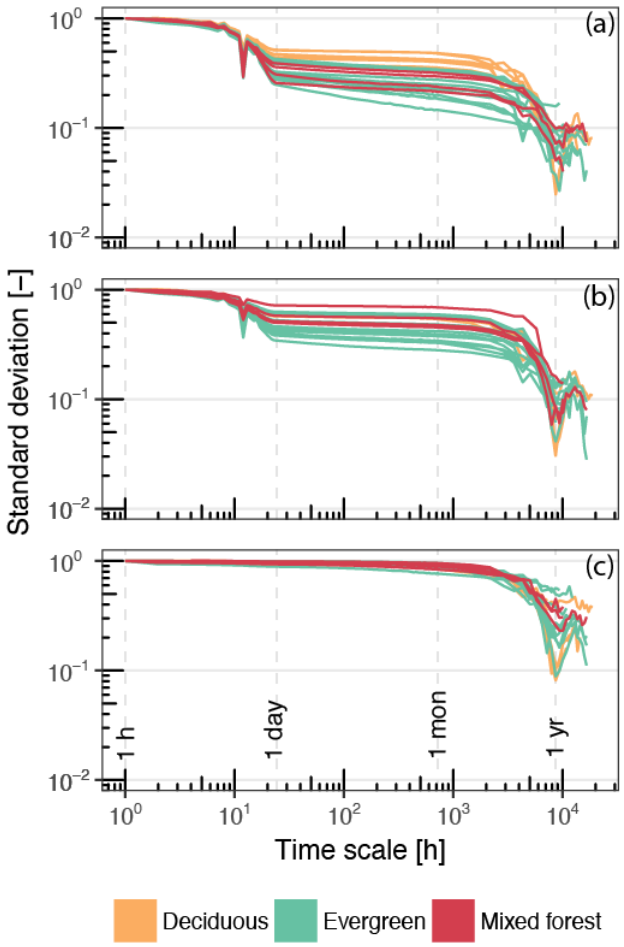

Figure S3. Variability of carbon fluxes measured (i.e., NEE; subplot a) and inferred (GPP, RECO; subplots b and c, respectively) with the eddy covariance technique at the 23 analysed sites. Standard deviation is illustrated as a function of the averaging time scale from hourly to interannual scales. Data are standardized, i.e., zero mean and unit variance, at the hourly time scale, so that patterns of variability can be compared across sites. Different colours correspond to different forest types.

S1.2 Reanalysis hydrometeorological data

S1.2.1 ERA Interim

ERA Interim product [*Dee et al.*, 2011] is a global gridded dataset that provides daily values of several climatological variables with a spatial resolution of 0.125° x 0.125°. Data for the period 1974 to 2014 downloaded from http://apps.ecmwf.int/datasets/data/interim-full-daily. The following variables are used in our analysis: 2-metre dew point temperature, surface pressure, surface net solar radiation, 2-metre temperature, and precipitation. VPD is calculated using air temperature, and dew point temperature, following Clausius-Clapeyron equation, as described in *Bolton*, 1980.

S1.2.2 NCEP I, II

NCEP I [*Kalnay et al.*, 1996] and NCEP II [*Kanamitsu et al.*, 2002] products have a spatial resolution of 2.5° x 2.5° and a temporal resolution of 6 h. NCEP I covers the period 1948 till present (data till 2015 are used in our analysis), while NCEP II the period 1979 till present (data till 2015 are used in our analysis). For both datasets the following variables are used: precipitation, air temperature, downward solar radiation, air specific humidity, and air pressure. VPD is calculated using air temperature, air pressure, and air specific humidity, following Clausius-Clapeyron equation, as described in *Bolton*, 1980. Data provided by the NOAA/OAR/ESRL PSD, Boulder, Colorado, USA and downloaded with the R package RNCEP [*Kemp et al.*, 2012].

S1.2.3 20th Century Reanalysis Version v2c

The 20th Century Reanalysis [*Whitaker et al.*, 2004; *Compo et al.*, 2006, 2011] Version v2c has a spatial resolution of 2.0° x 2.0° and a temporal resolution of 3 h. It provides climatological data for the period 1851 to 2014. The following variables are used: 2-metre temperature, downward solar radiation, precipitation, air pressure at the surface, and specific humidity. VPD is calculated using air temperature, air pressure, and air specific humidity, following Clausius-Clapeyron equation, as described in *Bolton*, 1980. Data provided by the NOAA/OAR/ESRL PSD, Boulder, Colorado, USA, from their Web site at http://www.esrl.noaa.gov/psd/.

S1.2.4 CRU TS 1.2

CRU TS 1.2. product [*Mitchell et al.*, 2004] provides monthly gridded time series of climate data for the period 1901 to 2000 with a spatial resolution of 10'. The following variables are used: precipitation, air temperature, and vapour pressure. VPD is calculated from vapour pressure and air temperature, following Clausius-Clapeyron equation, as described in *Bolton*, 1980. Data downloaded from: https://crudata.uea.ac.uk/cru/data/hrg/timm/grid/CRU_TS_1_2.html.

S1.2.5 CRU TS 3.23

The CRU TS 3.23 dataset [*Harris et al.*, 2014] consists of monthly gridded climatological data from the period 1901 to 2014 with a spatial resolution of 0.5^{o} x 0.5^{o}. The following variables are used: precipitation, air temperature, and vapour pressure. VPD is calculated from vapour pressure and air temperature, following Clausius-Clapeyron equation, as described in *Bolton*, 1980. Data downloaded from https://crudata.uea.ac.uk/cru/data/hrg/cru_ts_3.23/.

S1.2.6 CRU-NCEPv4

The CRU-NCEPv4 product (available online: http://dods.extra.cea.fr/data/p529viov/cruncep/) is a combination of CRU TS3.21 (*Harris et al.*, 2014; 0.5°x0.5° monthly climatology covering the period 1901 to 2009) and NCEP I reanalysis product [*Kalnay et al.*, 1996]. It provides hydrometeorological data for the period 1901-2010 with a temporal resolution of six hours and a spatial resolution of 0.5^{o} x 0.5^{o}. The following variables are used: precipitation, air temperature, incoming shortwave radiation, air specific humidity, and air pressure. VPD is calculated using air temperature, air pressure, and air specific humidity, following Clausius-Clapeyron equation, as described in *Bolton*, 1980.

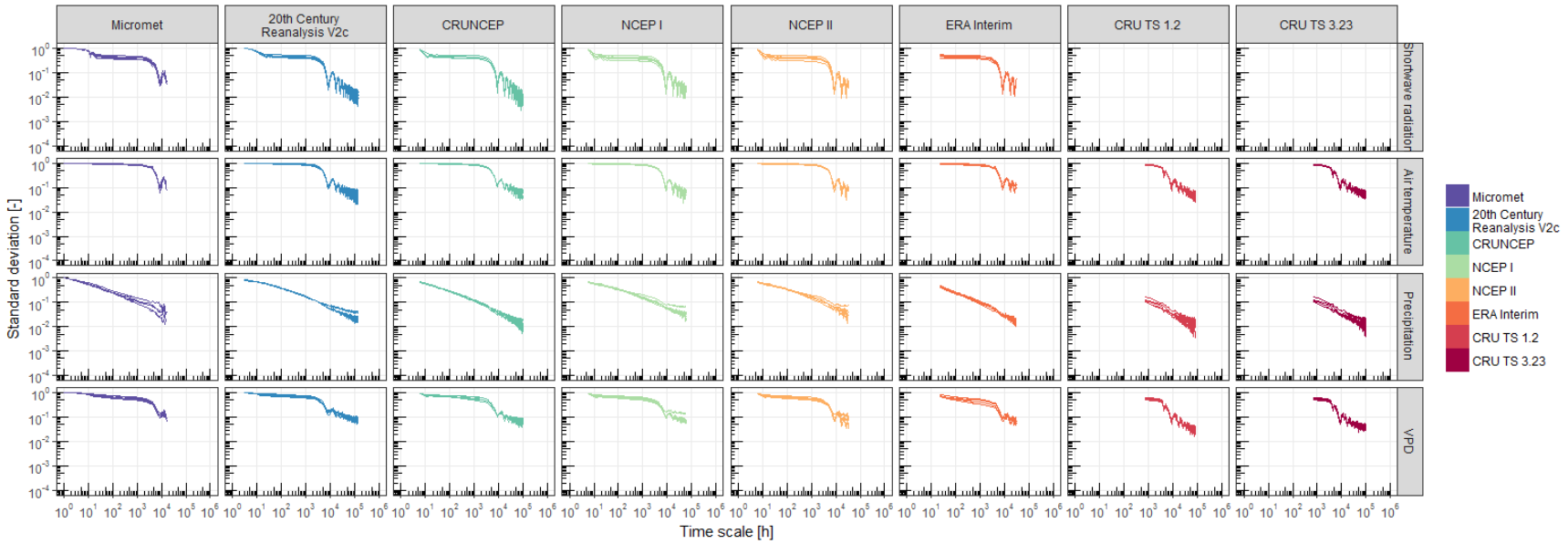

Figure S4. Standard deviation of shortwave radiation, air temperature, precipitation, and VPD, (y-axes; rows) as a function of the averaging time scale (x-axes) for different hydrometeorological datasets (columns and different colours; see Table S2) for the five European sites (BE-Bra, DE-Tha, DK-Sor, FI-Hyy, and IT-SRo; see Table S3).

S1.3 Remote sensing data

S1.3.1 MODIS TIP LAI and FPAR

Monthly values of Leaf Area Index (LAI) and Fraction of Photosynthetically Active Radiation (FPAR) from 2001 to 2014 (Figure S5), derived from MODIS and the Joint Research Centre Two-stream Inversion Package (JRC-TIP), are used [*Pinty et al.*, 2011]. The original data have a time step of 15 days and have been gap-filled for the cutouts at the FLUXNET stations according to a two-step procedure. First, we used distance correlations to identify nearby pixels with similar FPAR dynamics and used these values as estimates for the central pixel, if the distance correlations are ≥0.85. The remaining gaps were filled using the procedure proposed by *Kondrashov and Ghil*, 2006 in the exact setting as described by *Buttlar et al.*, 2014. More details on this product can be found in http://www.qa4ecv.eu/ecv/laifapar.

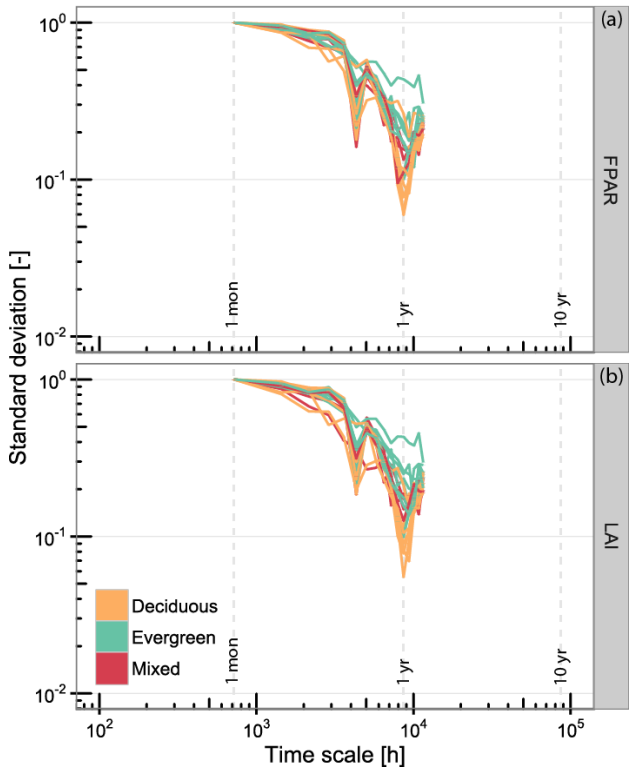

Figure S5. Standard deviation of the Fraction of Photosynthetically Active Radiation (FPAR; subplot a) and Leaf Area Index (LAI; subplot b) as a function of the averaging time scale, for the 20 sites based on the MODIS TIP dataset (sites AU-Tum, IT-SRo, and US-Blo are excluded due to low quality data of the corresponding grid cells; Table S3). Different colours depict different forest types. Note that time series are standardized (i.e., zero mean and unit variance) at the monthly time scale.

S1.3.2 GIMMS LAI3g and FPAR3g

Monthly values of Leaf Area Index (LAI 3g product) and Fraction of Photosynthetically Active Radiation (FPAR 3g product) for the period 1981-2011, are used [*Zhu et al.*, 2013]. LAI 3g and FPAR 3g show very similar patterns of change of variance as a function of the time scale (Figure S6). LAI 3g and FPAR 3g are derived from the Global Inventory Modelling and Mapping Studies

(GIMMS) Normalized Difference Vegetation Index (NDVI3g) [see *Zhu et al.*, 2013 for a detailed description].

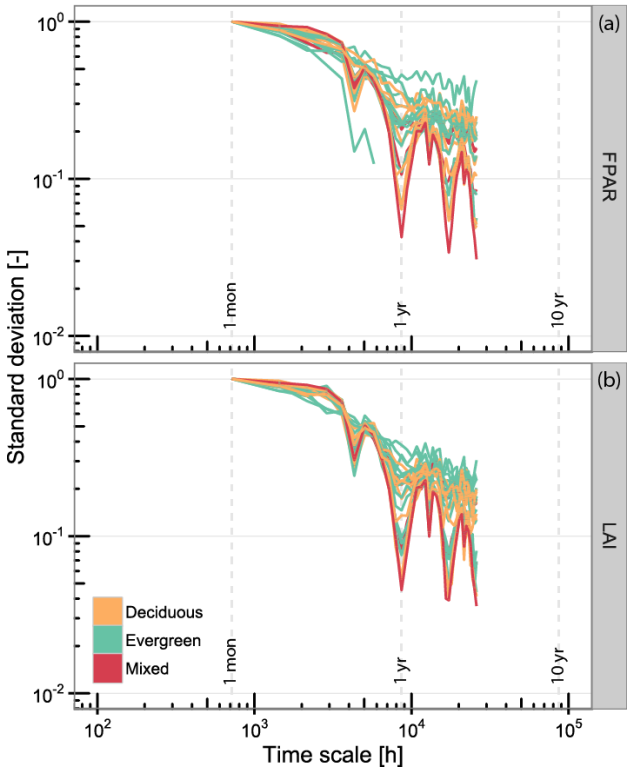

Figure S6. Standard deviation of the Fraction of Photosynthetically Active Radiation (FPAR 3g; subplot a) and Leaf Area Index (LAI 3g; subplot b) as a function of the averaging time scale, for the 23 sites (summarized in Table S3), based on the GIMMS dataset. Different colours depict different forest types. Note that the time series are standardized (i.e., zero mean and unit variance) at the monthly time scale.

S1.4 Tree-ring width and biomass data

To further investigate ecosystem variability at the interannual to decadal time scales, we incorporate in our analysis dendrochronological records available at five European forest sites covering different climatic zones and vegetation characteristics (Table S3; *Babst et al.*, 2014a, 2014b). More specifically, tree-ring width measurements and biometric data (Diameter at the Breast Height, DBH, tree height) were obtained from all trees with DBH > 5.6 cm (N ~50) within fixed-size plots located within the footprint area of the eddy covariance flux tower at these five European forests, as described in *Babst et al.*, 2014a, 2014b (Table S3).

Tree-ring width measurements provide a direct quantification of annual radial stem growth at each site (Figure S7). Furthermore, above ground woody biomass estimates, derived by *Babst et al.*, 2014a, 2014b, using tree-ring widths, biometric measurements, and species-specific allometric equations, provide an ecosystem-level description of the annual forest biomass dynamics (Figure S8). *Babst et al.*, 2014a, 2014b investigated and confirmed the regional representation of the identified tree growth dynamics as quantified by the tree-ring chronologies. The tree-ring width chronologies are derived using the dplR package [http://cran.r-project.org/package=dplR; *Bunn*,

2008, 2010]. The shortest chronology covers the period 1969 to 2009 (FI-Hyy), while the longest one covers a period of 111 years (1899-2009; DE-Tha), Figure S7Figure S8.

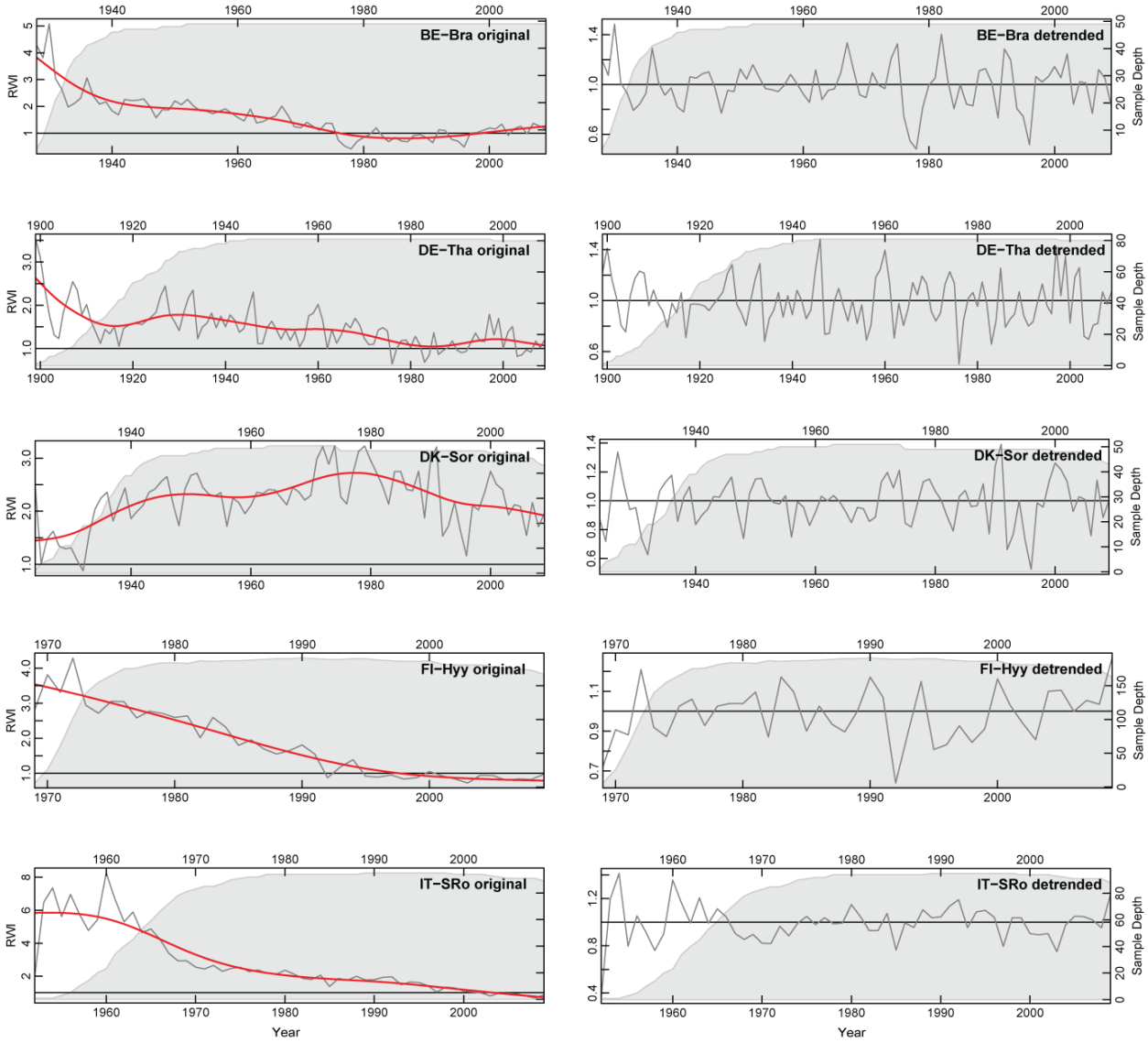

Figure S7. Tree-ring derived chronologies (original and detrended time series) for the five locations across Europe with eddy covariance flux towers (see Table S3). Tree-ring width indices (RWI) are shown on the left-hand side while the sample depth is on the right-hand side of the vertical axes. The solid red line highlights the cubic smoothing spline (50% frequency cutoff response at 30 years) that is applied for the detrending.

A common practice in dendroclimatology is to derive tree-ring index chronologies after detrending the tree-ring width measurements (Figure S7; *Fritts*, 1976). Detrending is the post-processing of the tree-ring width measurements to remove age/size related signals from tree-ring width measurements [Figure S9; *Fritts*, 1976]. It has been observed that ring width generally decreases with tree age/size, leading to a biological and/or geometric age trend [*Fritts*, 1976; *Mencuccini et al.*, 2005]. A robust statistical description of age-related trends remains still challenging and different methods may lead to significantly different results [e.g., *Esper and Frank*, 2009; *Bowman*

et al., 2013]. *Peters et al.*, 2015 provide a review of commonly applied detrending methods. However, when the focus is on understanding the variability in tree growth, and the resulting ecosystem variability, any age-related trend could also be seen as an ontogenetic pattern, that reflects an inherent property of plant development. Thus, the original tree-ring width data are used. Our study uses two metrics for tree growth: the raw tree-ring width and the derived biomass data.

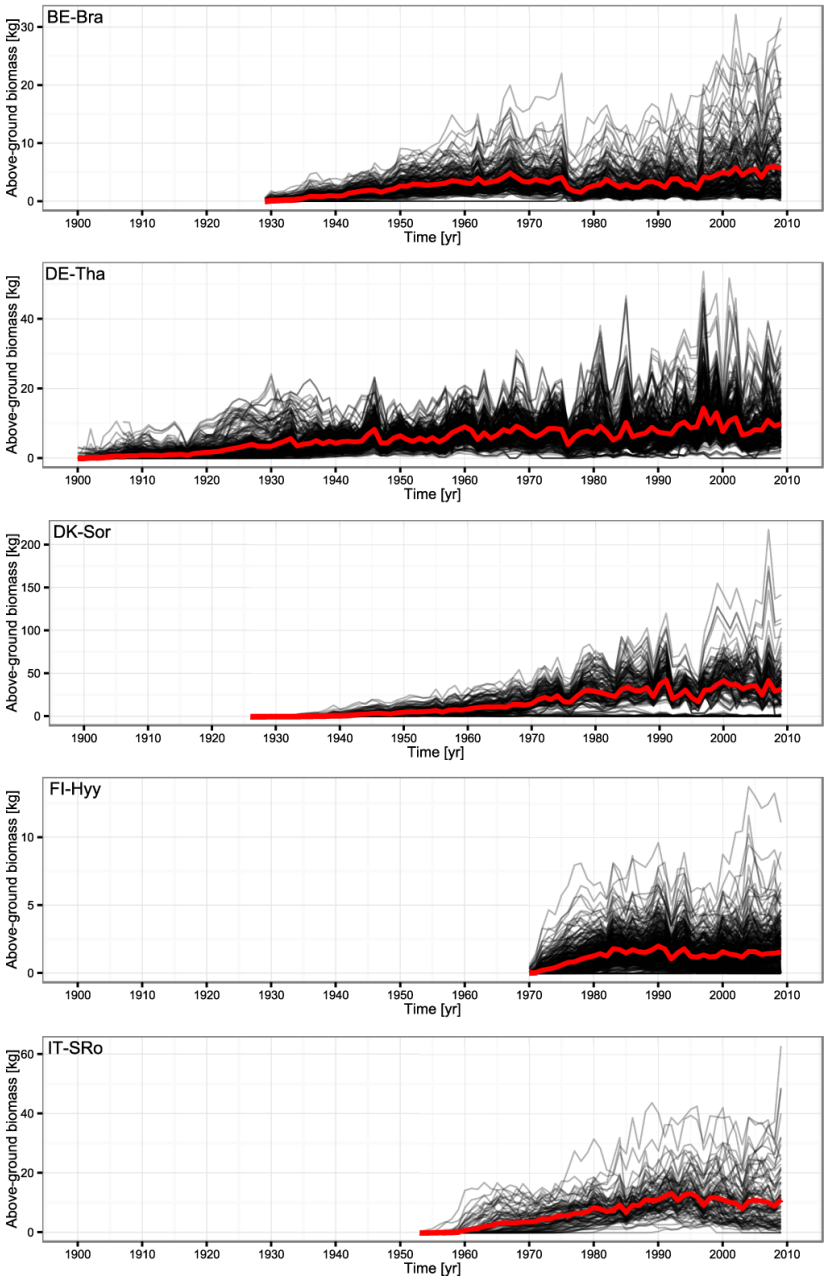

Figure S8. Annual increments of aboveground woody biomass of selected trees located at the footprint of five eddy covariance flux towers across Europe (Table S3). Black lines illustrate biomass estimates with various biomass allometric functions as detailed in *Babst et al.*, 2014a, 2014b, while red lines correspond to the mean of the distribution.

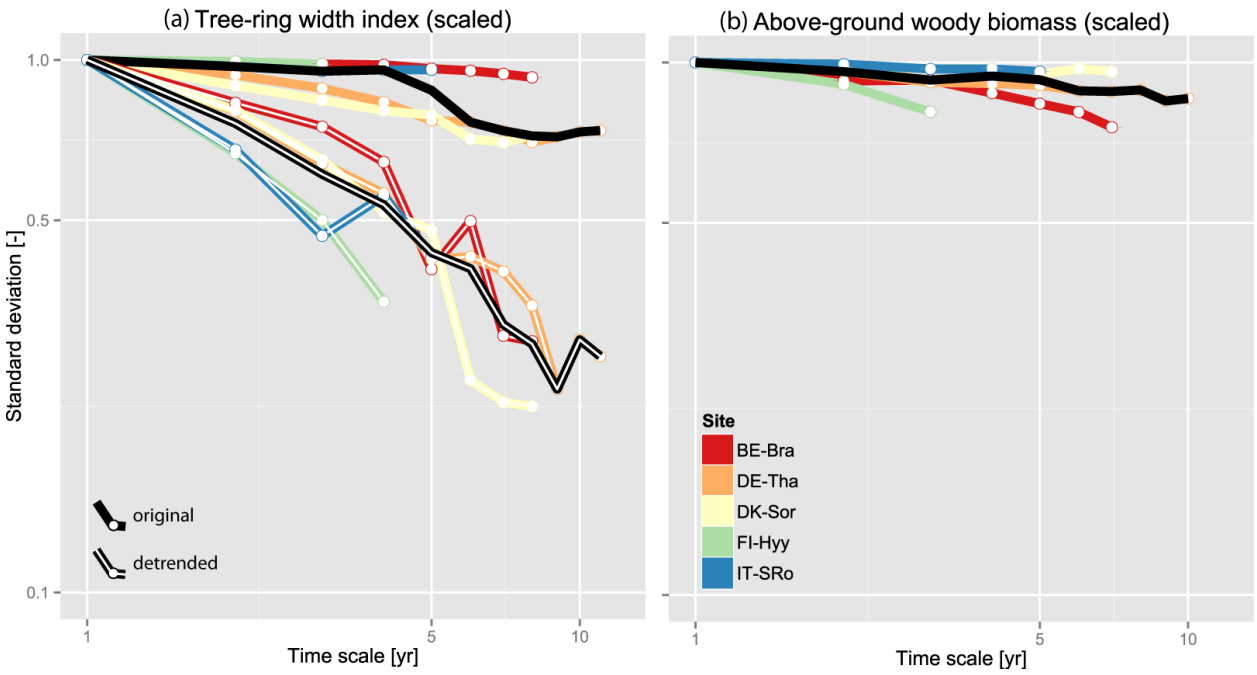

Figure S9. Standard deviation of the tree-ring width chronologies (subplot a) and above-ground woody biomass (subplot b) as a function of the averaging scale (x-axes) for the five examined locations (Table S3). Subplot (a) includes both the raw data (solid coloured lines) and the detrended chronologies (solid coloured lines with a white line in the middle). The median of the distributions across sites is depicted with a black line. Note that the time series are standardized (i.e., zero mean and unit variance) at the annual time scale.

S1.5 Agreement of ecosystem variability at the overlapping time scales of remote sensing and tree-ring width data

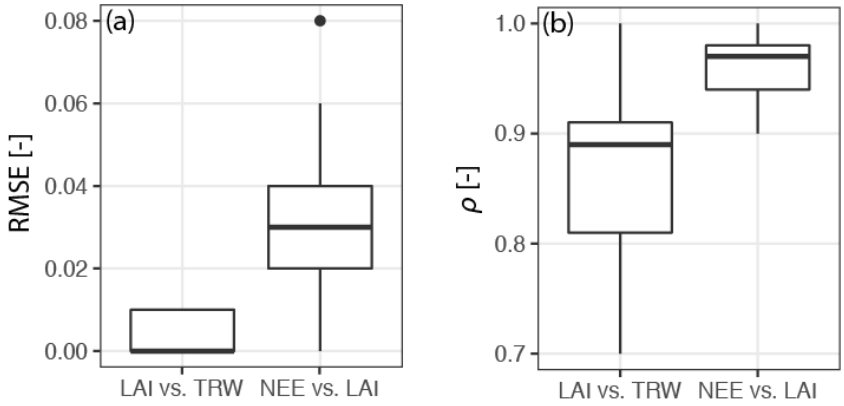

Figure S10. Boxplots of root mean square error (RMSE; subplot a) and correlation coefficient (ρ; subplot b) between the variability (standard deviation) of individual ecosystem variables (i.e., net ecosystem exchange, NEE, leaf area index, LAI from GIMMS 3g, and tree-ring widths, TRW) at the overlapping time scales of the ecosystem variability continuum for the 23 analysed sites. Note that while NEE and LAI data are available for all the analysed locations, TRW data are available only for five sites (see Table S3 and Figure 1 of the main text). Boxes are extended from 25% lower quartile ($q_{0.25}$) to 75% upper quartile ($q_{0.75}$) while whiskers represent the range of [$q_{0.5}$ - 1.5 IQR, $q_{0.5}$ + 1.5 IQR], where $q_{0.5}$ is the median and IQR is the interquartile range ($q_{0.75}$ - $q_{0.25}$).

S1.6 TRENDY multi-model outputs

Monthly values of terrestrial CO_2 exchange from the multi-model output of the TRENDY project (Trends in net land atmosphere carbon exchanges, *Le Quéré et al.*, 2013; *Piao et al.*, 2013; *Sitch et al.*, 2015; http://dgvm.ceh.ac.uk/) are analysed. The data are available from http://www-lscedods.cea.fr/invsat/RECCAP/. The analysed results correspond to simulations with changing CO_2 and climate for the period 1901-2010 (S2 experiment). The following DGVMs participated in the TRENDY project: Hyland, TRIFFID/JULES, LPJ, LPJ-GUESS, NCAR-CLM4, ORCHIDEE, OCN, SDVGM, VEGAS. However, for our analysis, simulation results with Hyland are discarded since they have annual time step, while all the other models provide monthly outputs. The analysed results correspond to the period is from 1901 to 2010 (i.e., spin up and historical period), with the exception of ORCHIDEE that the analysed period is from 1981 to 2010. In addition, the coordinates of two of the examined sites (BE-Bra and DK-Sor; see Table S3) fall out of the terrestrial grid in the simulations with TRIFFID/JULES due to its coarse spatial resolution (3.75^o x 2.5^o). Thus, for these two specific sites, simulation results with TRIFFID/JULES are discarded.

The CRU-NCEPv4 product (http://dods.extra.cea.fr/data/p529viov/cruncep/; see section S1.2.6 for a detailed product description) is used as climate forcing (e.g., precipitation, air temperature, radiation) for the TRENDY multi-model simulations (Figure S11). Net Biospheric Production (NBP; NBP=-NEE) simulated with several Dynamic Global Vegetation Models (DGVMs), part of TRENDY v1 output, is used for describing the simulated continuum of ecosystem variability since it is closely related with the observed ecosystem variables used in the composite ecosystem variability continuum (Figure S12 and Figure 5 of the main text).

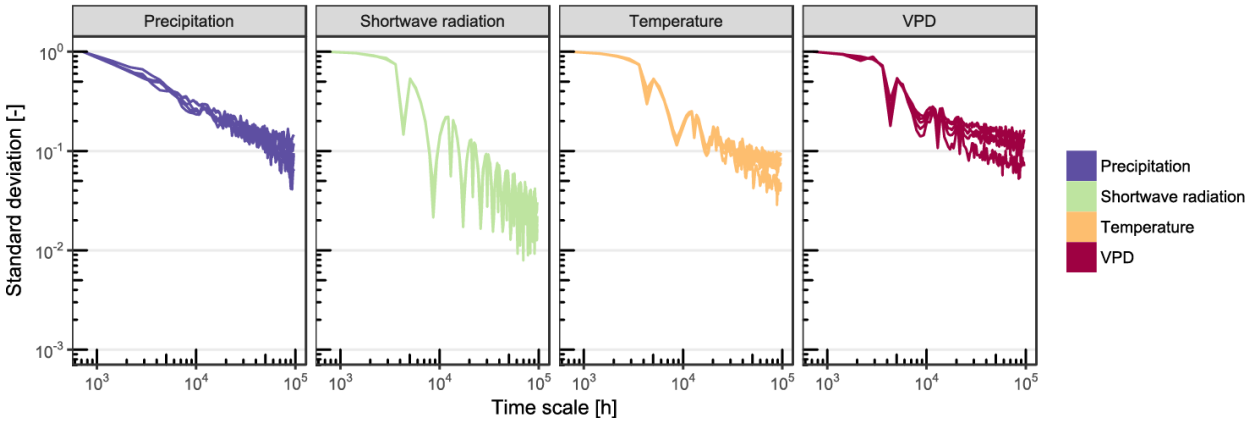

Figure S11. Standard deviation of the climate input (TRENDY meteorological forcing; precipitation, shortwave incoming radiation, air temperature, and vapour pressure deficit, VPD from the CRU-NCEPv4 product) as the function of the averaging time scale, from one month to about one decade. The data correspond to five of the examined sites (BE-Bra, DE-Tha, DK-Sor, FI-Hyy, IT-SRo; see Table S3). Note that the time series are standardized (i.e., zero mean and unit variance) at the monthly time scale.

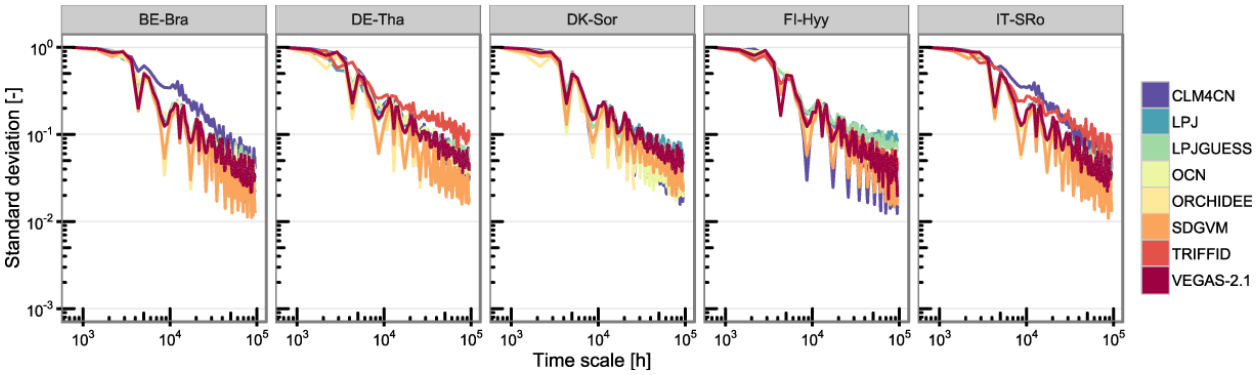

Figure S12. Standard deviation of NEE as a function of the averaging time scale (from one month to about one decade) for five European sites (see Table S3) based on the TRENDY multi-model simulation results. Different colours depict different Dynamic Global Vegetation Models (DGVMs). Note that the time series are standardized (i.e., zero mean and unit variance) at the monthly time scale.

In addition, the variability of individual components of NEE, consisting of simulated Gross Primary Productivity (GPP), Net Primary Productivity (NPP), and heterotrophic respiration (RH) is also illustrated in Figure S13 (see *Chapin et al.*, 2006 for detailed definitions of variables describing terrestrial carbon fluxes and stocks). GPP and NPP show similar patterns of variability, highlighting the carbon-centric structure of DGVMs in simulating forest growth [e.g., *Sala et al.*, 2012; *Pappas et al.*, 2013; *Fatichi et al.*, 2014; *Körner*, 2015], while RH follows closely the pattern of variability of temperature (upper limit of the hydrometeorological envelope), as a result of the close dependence of RH to temperature that is incorporated in DGVMs [e.g., *Sitch et al.*, 2003; *Oleson et al.*, 2013; *Ballantyne et al.*, 2017].

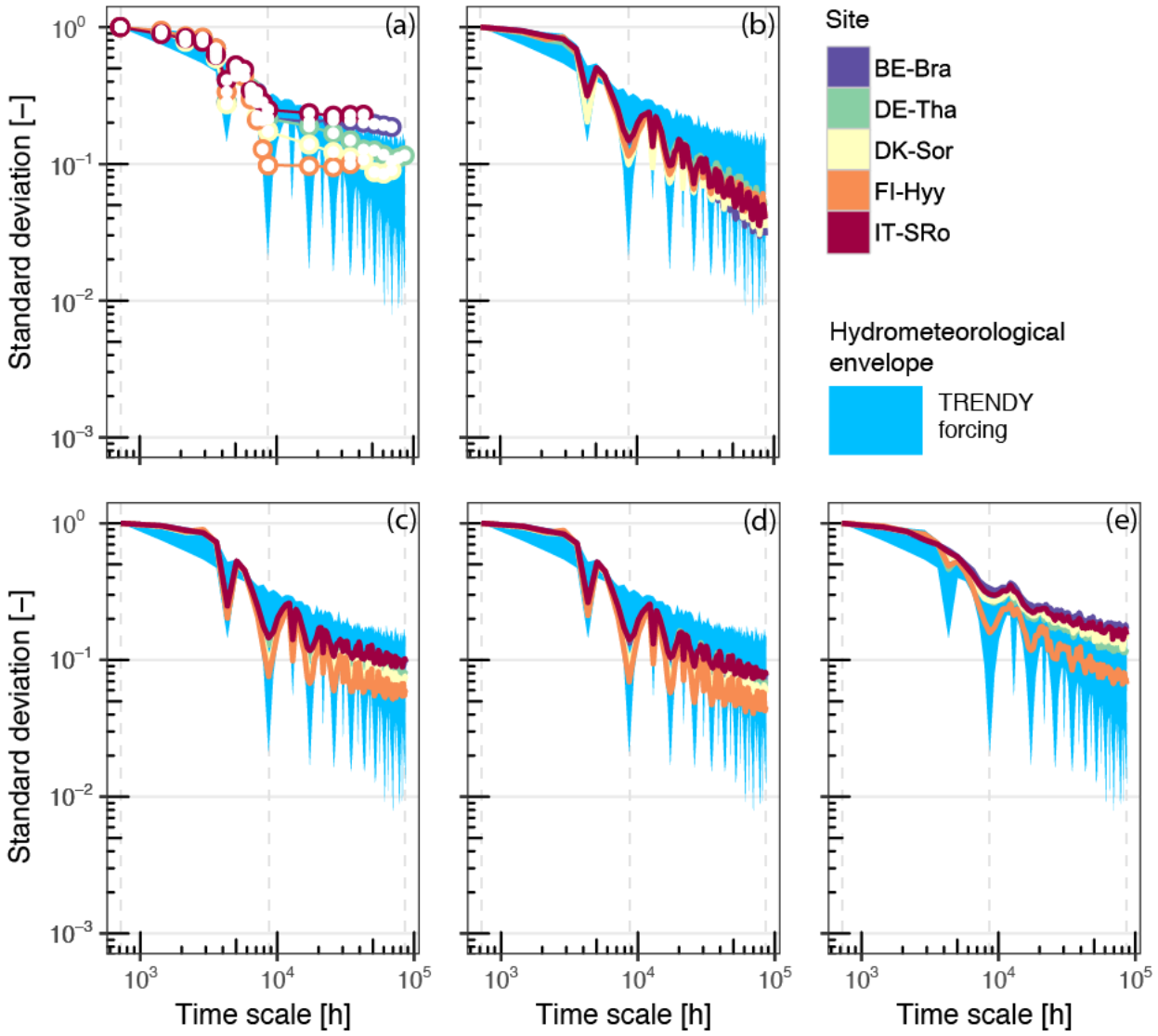

Figure S13. A comparison of observed (subplot a) and simulated (TRENDY multi-model mean simulated NEE; subplot b) ecosystem variability across the five European sites (see Table S3; coloured lines), as well as additional simulated ecosystem variables, namely GPP (subplot c), NPP (subplot d), and RH (subplot e). The shaded area denotes the hydrometeorological envelope of the TRENDY climate forcing (CRU-NCEPv4). For figures' clarity, data are standardised so that they have zero mean and unit variance at the monthly time scale. Standard deviation of NEE as a function of the averaging time scale (from one month to about one decade) based on the TRENDY multi-model simulation results. Different colours depict different Dynamic Global Vegetation Models (DGVMs). Note that the time series are standardized (i.e., zero mean and unit variance) at the monthly time scale. Note that subplots a and b are the same as Figure 5a,b of the main text.

S2 Empirical climacograms

S2.1 Mean climacograms of hydrometeorological variables

The climacogram of each hydrometeorological variable (precipitation, air temperature, radiation, VPD) is calculated as the mean over micrometeorological and reanalysis data with fine temporal resolution (CRU-NCEPv4 and 20th century reanalysis products; Figure S14).

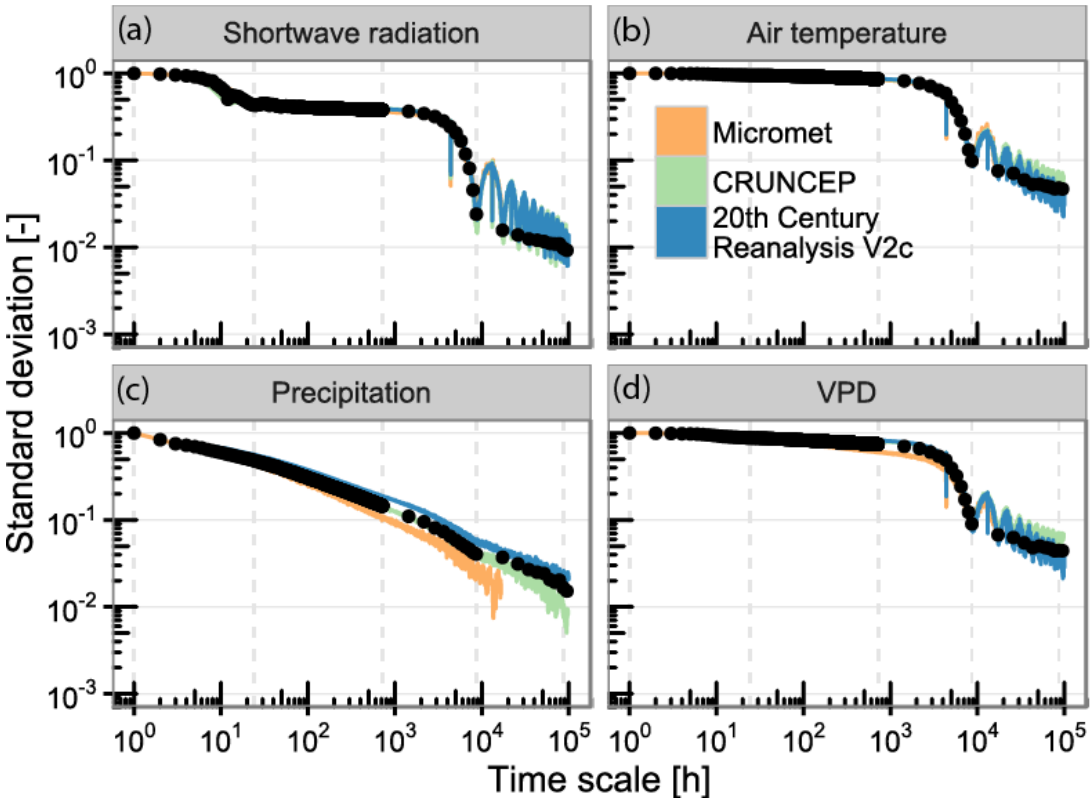

Figure S14. Mean empirical climacograms (black dots) of the analysed climatic variables for an exemplary site (DE-Tha, see Table S3), namely (a) shortwave radiation, (b) air temperature, (c) precipitation, and (d) VPD. Coloured lines indicate different datasets: micrometeorological data with hourly time step, reanalysis data clipped at the DE-Tha site with six- and three-hour time step, CRU-NCEPv4 and 20th century reanalysis, respectively.

S3 Model fitting

The model structure that describes best the observed dynamics of the hydroclimatic and ecosystem variability (i.e., the relation of standard deviation as a function of averaging time scale; $\sigma_y^{(k)}$) is the linear combination the diurnal (T_1=24 h) and seasonal (T_2=1 yr) cycle harmonics ($\sigma_{T_1}^{(k)}$ and $\sigma_{T_2}^{(k)}$, respectively) and a process with long-term persistence ($\sigma_{\mathrm{HK}}^{(k)}$), i.e.,

$$\sigma_y^{(k)} = a\sigma_{T_1}^{(k)} + b\sigma_{T_2}^{(k)} + c\sigma_{\mathrm{HK}}^{(k)}$$

where a, b, and c are weighting factors (Figure 6c, d, in the main text).

Figure S15 summarizes the distribution of the slopes in the climacograms of hydrometeorological and ecosystem variables, θ, where θ=H-1 with H denoting the Hurst coefficient across the 23 sites (Table S3).

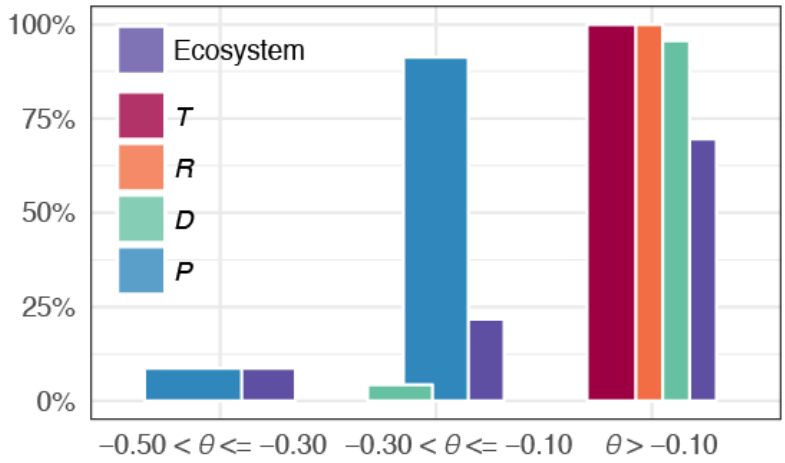

Figure S15. Distribution of the slopes of the climacograms (θ=H-1, where H is the Hurst coefficient), for the 23 analysed sites (Table S3) for climate forcing (air temperature, T, shortwave radiation, R, vapour pressure deficit, D, and precipitation, P) and ecosystem response. For the five sites where tree rings are available the fitting was made to NEE, LAI 3g, and TRW data, while for the remaining sites the fitting was made only to NEE, and LAI 3g data.

S4 Standard deviation of a deterministic single harmonic process as a function of the averaging time scale

Given a deterministic periodic process, $x(t)$, of a single harmonic with period T

$$x(t) = \sqrt{2}\cos\left(\frac{2\pi t}{T} + b\right) \tag{S.1}$$

where t is time and $b \in [0, \pi]$ is the phase (horizontal shift in Figure S16), we can derive analytically how the standard deviation (σ) of this process (and also that of other structurally similar processes) changes as a function of the averaging time scale (k).

Here, we will revise the proof presented by *Markonis and Koutsoyiannis*, 2012, in order to show that for a single harmonic process, described by Equation (S.1), there is:

(i) a drop in σ at averaging time scales of k=aT, where $a \in \mathbf{N}$ (as predicted by *Markonis and Koutsoyiannis*, 2012),

(ii) but also a discontinuity in σ at specific averaging time scales, corresponding to k=(m+1/2)T where $m \in \mathbf{N}^0$. This discontinuity can be explained by either the symmetric shape of the harmonic function (leading to a local abrupt drop in σ) or due to the starting point of the integration of the harmonic signal, i.e., caused by the horizontal drift (parameter b) or the data availability (parameter c, see below), leading to local abrupt changes of σ at averaging scales of k=(m+1/2)T.

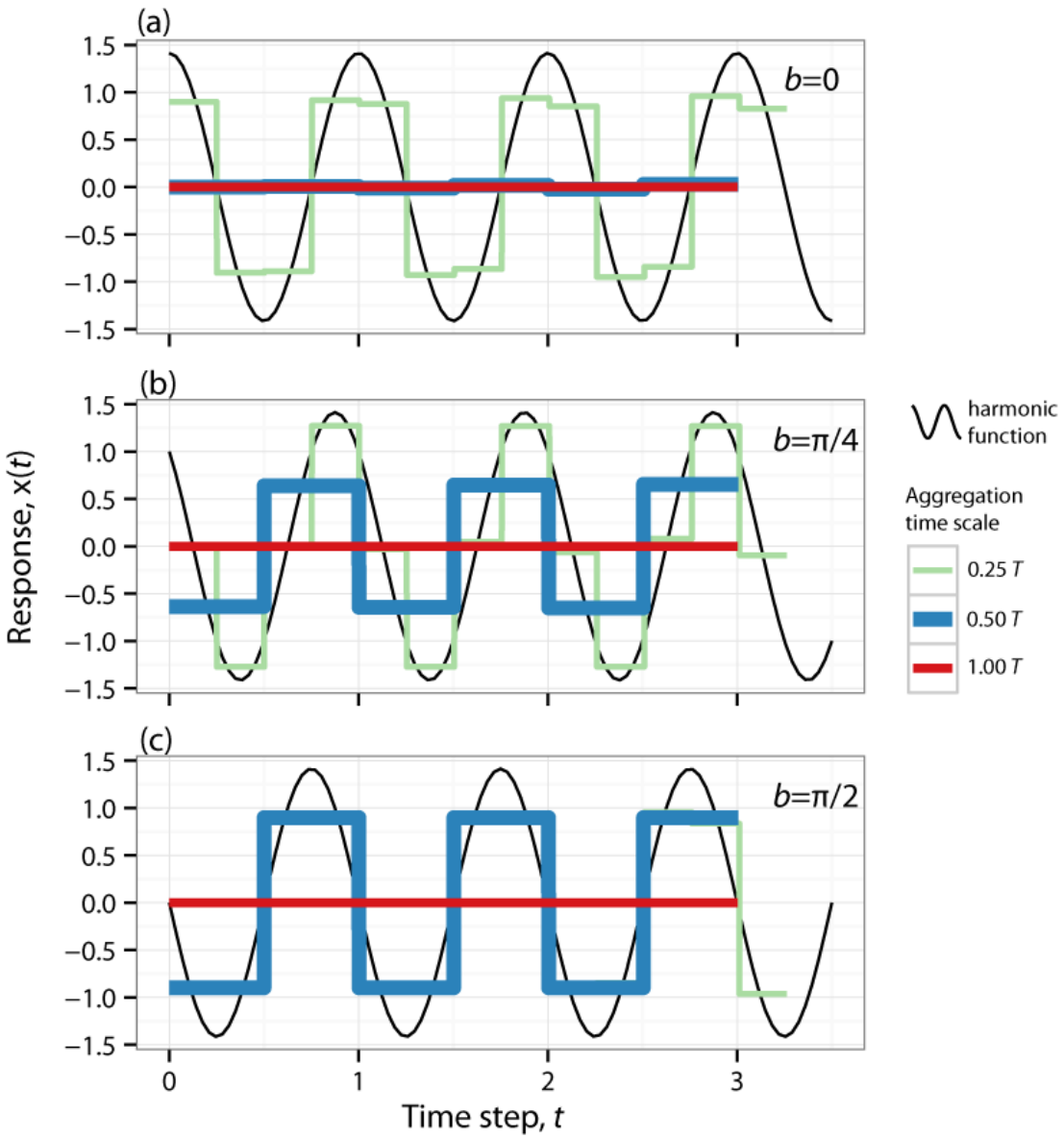

Figure S16. Time series of a deterministic periodic process of a single harmonic with period T=1, described by Equation (S.1) and the time series of the averaged process at selected time scales corresponding to T/4, T/2, and T. Subplots (a), (b), and (c) correspond to different values of parameter b (horizontal phase shift; see Equation (S.1)). For illustration purposes $t \in [0,4]$ and the amplitude of the harmonic is $\sqrt{2}$. At averaging scales of $k=aT$, where $a \in \mathbf{N}^+$, the standard deviation of the averaging process (red solid line) is minimum (flat line). Furthermore, for b=0 (subplot (a)) the standard deviation at averaging scales of $k=(m+1/2)T$ where $m \in \mathbf{N}^0$ coincides with that of averaging scales of $k=aT$, where $a \in \mathbf{N}^+$ (i.e., minimum; solid blue line). Interestingly, for $b=\pi/4$ or $b=\pi/2$ the standard deviation of the averaging process for scales of $k=(m+1/2)T$ is greater than zero (solid blue lines in subplots (b) and (c)). Note that in subplot (c) green and blue lines overlap.

After integrating Equation (S.1) at time scale T/2 (solid blue line in Figure S16), denoting $x_{t_1}^{(k=T/2)}$ the average of $x(t)$ in $[c, c+T/2]$, $x_{t_2}^{(k=T/2)}$ the average of $x(t)$ in $[c+T/2, c+T]$, ..., $x_{t_N}^{(k=T/2)}$ the average of $x(t)$ in $[c+NT/2, c+(N+1)T/2]$, where $c \in [0, T/2]$, and $N \in \mathbf{N}^+$, we obtain:

$$x_{t_1}^{(k=T/2)} = \frac{2}{T}\int_{c}^{c+T/2} x(t)dt = \frac{2}{T}\int_{c}^{c+T/2} \sqrt{2}\cos\left(\frac{2\pi t}{T}+b\right)dt = -\frac{2\sqrt{2}}{\pi}\sin\left(\frac{2\pi c}{T}+b\right)$$

$$x_{t_2}^{(k=T/2)} = \frac{2}{T}\int_{c+T/2}^{c+T} x(t)dt = \frac{2}{T}\int_{c+T/2}^{c+T} \sqrt{2}\cos\left(\frac{2\pi t}{T}+b\right)dt = \frac{2\sqrt{2}}{\pi}\sin\left(\frac{2\pi c}{T}+b\right)$$

...

$$x_{t_N}^{(k=T/2)} = \frac{2}{T}\int_{c+N(T/2)}^{c+(N+1)T/2} x(t)dt = \frac{2}{T}\int_{c+NT/2}^{c+(N+1)T/2} \sqrt{2}\cos\left(\frac{2\pi t}{T}+b\right)dt = -\frac{2\sqrt{2}}{\pi}\sin\left(\pi\left(\frac{2c}{T}+N\right)+b\right)$$

Thus,

$$x_{t_i}^{(k=T/2)} = \begin{cases} -\frac{2\sqrt{2}}{\pi}\sin\left(\frac{2\pi c}{T}+b\right), \text{for } i = 0,2,4,... \\ \frac{2\sqrt{2}}{\pi}\sin\left(\frac{2\pi c}{T}+b\right), \text{for } i = 1,3,5,... \end{cases} \quad \text{(S.2)}$$

Equation (S.2) implies that the mean of $x_{t_i}^{(k=T/2)}$ is equal to zero, i.e., $\mu_{x_t^{(k=T/2)}} = 0$. The standard deviation of the averaged process at the time scale of $k=T/2$ is then given by:

$$\sigma^{(k=T/2)} = \sqrt{\mathrm{Var}(x_{t_1}^{(k=T/2)}, x_{t_2}^{(k=T/2)}, ..., x_{t_N}^{(k=T/2)})} = \sqrt{\mathrm{E}\left[\left(x_t^{(k=T/2)} - \mu_{x_t^{(k=T/2)}}\right)^2\right]} = \sqrt{\mathrm{E}\left[\left(x_t^{(k=T/2)}\right)^2\right]}$$

$$\Rightarrow \sigma^{(k=T/2)} = \frac{2\sqrt{2}}{\pi}\left|\sin\left(\frac{2\pi c}{T}+b\right)\right| \quad \text{(S.3)}$$

Equation (S.3) predicts the change in standard deviation of a periodic process with period T, as described by Equation (S.1), at averaging scales of $k=T/2$, $3T/2$, $5T/2$,..., $(m+1/2)T$ where $m \in \mathbf{N}^0$. Equation (S.3) has a minimum equal to zero and a maximum equal to $2\sqrt{2}/\pi$. The dependence of $\sigma^{(k=T/2,..., (m+1/2)T)}$ to the parameters b and c is illustrated in Figure S17.

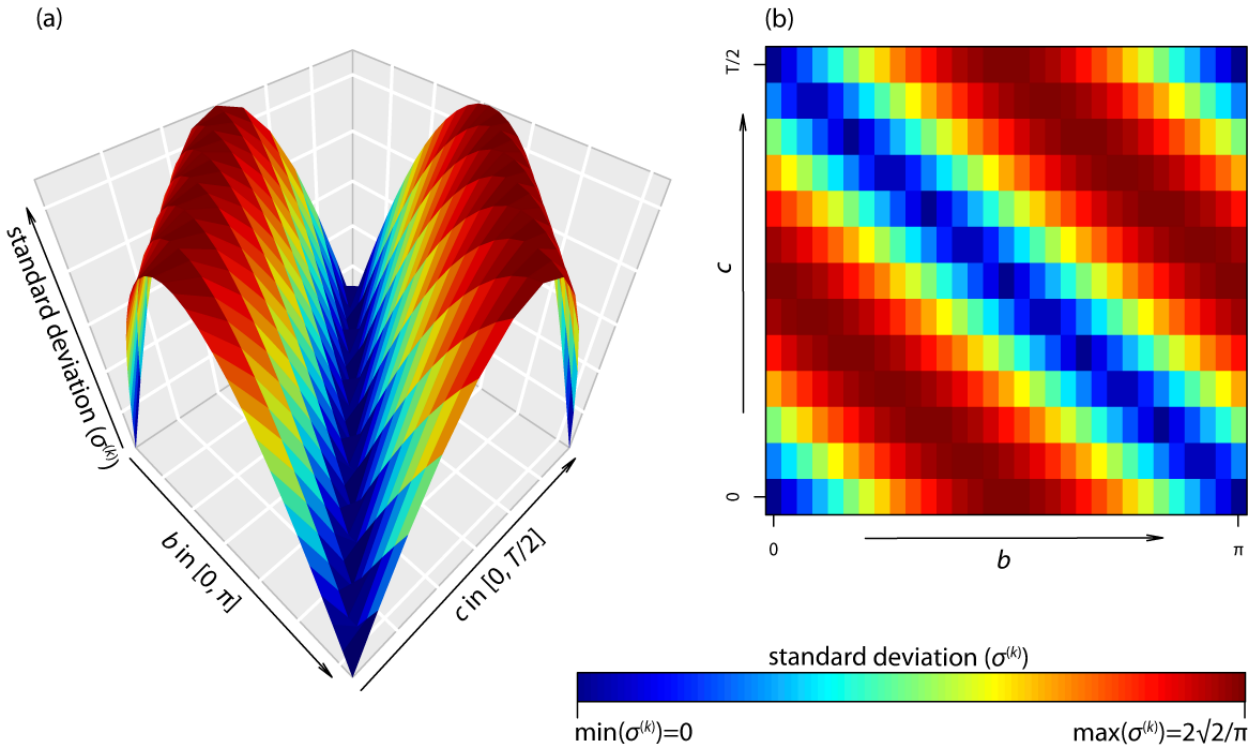

Figure S17. Standard deviation (σ) of deterministic periodic process, with period T, described by Equation (S.1), at averaging time scales of $k=T/2, 3T/2, 5T/2,..., (m+1/2)T$ where $m \in \mathbf{N}^0$ as a function of parameters b and c, illustrated in the three- (subplot (a)) and two-dimensional space (subplot (b)). Note that depending on the parameters b and c the standard deviation at scales $k=T/2, 3T/2, 5T/2,..., (m+1/2)T$, can vary from 0 (i.e., $\min(\sigma^{(k)})$) to $2\sqrt{2}/\pi$ (i.e., $\max(\sigma^{(k)})$). For example, in the exemplary time series presented in Figure S16, for $c=0$, $\sigma^{(k)}$ is minimum for $b=0$ (Figure S16a) or $b=\pi$, and $\sigma^{(k)}$ is maximum for $b=\pi/2$ (Figure S16c).

In order to illustrate how the aforementioned findings are reflected in our analysis, we generated synthetic time series of hourly values with 10 years length (i.e., 86400 data points) using Equation (S.1), with period $T=24$. Thus, we mimic the diurnal harmonic that is also present in the data we analysed. In real case applications parameters b and c can have similar effects, i.e., a horizontal phase shift (reflected in parameter b) has the same effect in our averaging procedure as ignoring few values at the beginning of the time series and starting the integration at a time step $t+c$. Therefore, since in our analysis the averaging of the time series at different time scales starts always from the first available observation, we assume $c=0$ and we focus on the parameter b. Three different time series of a single harmonic with parameter b equal to π, $\pi/2$, and $\pi/4$, respectively, are generated and the relation between the standard deviation of these three time series as a function of the averaging scale is illustrated in Figure S18.

Markonis and Koutsoyiannis, 2012 have shown that for a periodic process described by Equation (S.1) the standard deviation of the averaging process as a function of the averaging time scale is given by:

$$\sigma^{(k)} = \frac{T}{\pi k}\left|\sin\frac{\pi k}{T}\right| \tag{S.4}$$

This relation describes the drop in standard deviation of periodic processes at averaging scales $k=aT$, where $a \in \mathbf{N}$. Our analysis revises their proof in order to account for a discontinuity in standard deviation at averaging time scales of $k=(m+1/2)T$ where $m \in \mathbf{N}^0$ (Equation (S.3)). The theoretical relation provided by *Markonis and Koutsoyiannis*, 2012 (solid black line; Figure S18) captures the exact pattern illustrated by the empirical estimates based on the synthetic data (coloured points) with the exception of specific averaging scales of $k=T/2, 3T/2, 5T/2,..., (m+1/2)T$ where $m \in \mathbf{N}^0$. For these specific averaging time scales the standard deviation of the averaging process varies in $[0, 2\sqrt{2}/\pi]$.

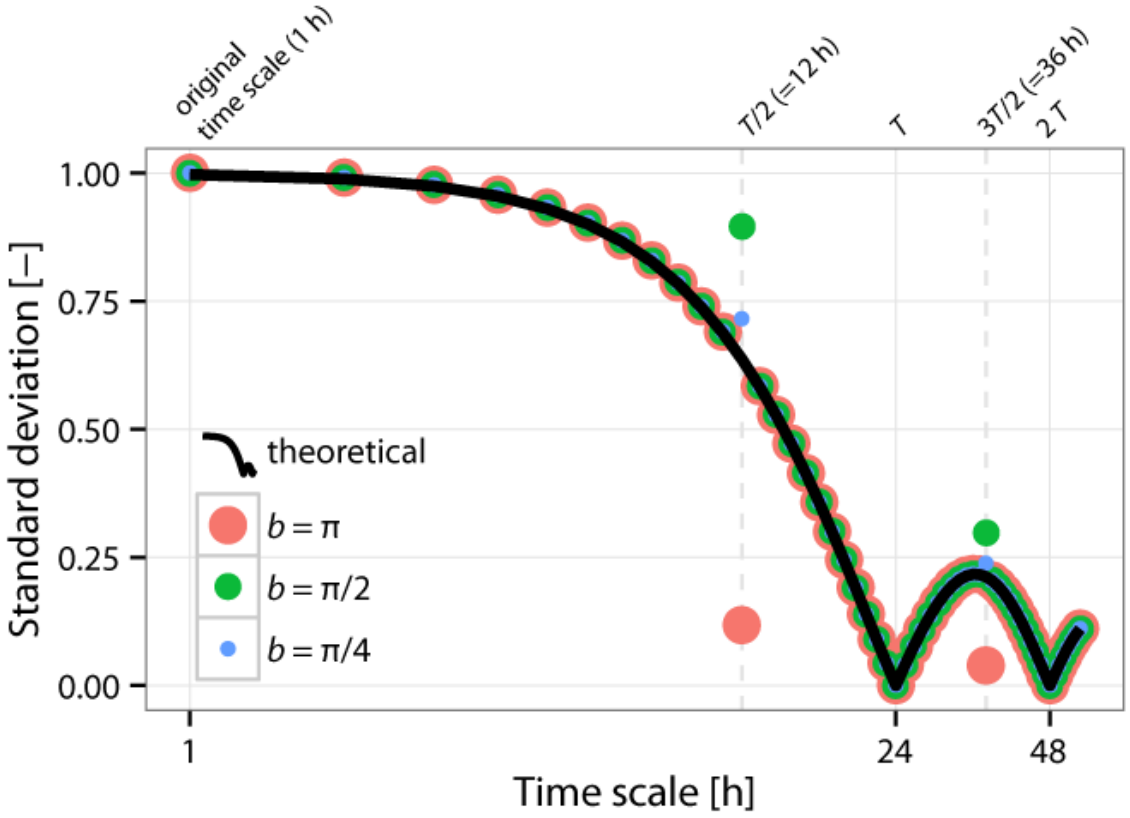

Figure S18. Standard deviation of synthetic time series of a deterministic single harmonic process described by Equation (S.1) for period T=24 h as a function of the averaging time scale for different values of parameter b (coloured points). The generated synthetic time series have hourly time step and length 10 years (i.e., 86400 data points). For the sake of clarity, the averaging time scale is extended up to 50 h (horizontal axis; log scale). The theoretical decay of the standard deviation with time scale based on *Markonis and Koutsoyiannis*, 2012 is also included (solid black line).

Parameters b and c in Equation (S.3) can be substituted by a single parameter u as follows:

$$\sigma^{(k=T/2)} = \frac{2\sqrt{2}}{\pi}\left|\sin\left(\frac{2\pi c}{T}+b\right)\right| = \frac{2\sqrt{2}}{\pi}\left|\sin\left(\frac{2\pi c}{T}+\frac{2\pi b'}{T}\right)\right| =$$

$$= \frac{2\sqrt{2}}{\pi} \left| \sin\left(\frac{2\pi}{T}(c + b')\right) \right| = \frac{2\sqrt{2}}{\pi} \left| \sin\left(\frac{2\pi}{T}u\right) \right|$$

where $b = \frac{2\pi b'}{T}$ and $u = c + b', u \in [0, T]$. Therefore, for a periodic process described by Equation (S.1) the standard deviation of the averaging process as a function of the averaging time scale is given by:

$$\sigma^{(k)} = \begin{cases} \frac{T}{\pi k} \left| sin \frac{\pi k}{T} \right|, \text{ for } k \neq \left(m + \frac{1}{2}\right) T, \text{where } m \in \mathbf{N}^0 \\ \\ \frac{2\sqrt{2}}{\pi} \left| \sin\left(\frac{2\pi}{T}u\right) \right|, \text{for } k = \left(m + \frac{1}{2}\right) T, \text{where } m \in \mathbf{N}^0 \text{ and } u \in [0, T] \end{cases} \quad \text{(S.5)}$$

References

Babst, F. et al. (2014a), Above-ground woody carbon sequestration measured from tree rings is coherent with net ecosystem productivity at five eddy-covariance sites, *New Phytol.*, *201*, 1289–1303, doi:10.1111/nph.12589.

Babst, F., O. Bouriaud, R. Alexander, V. Trouet, and D. Frank (2014b), Toward consistent measurements of carbon accumulation: A multi-site assessment of biomass and basal area increment across Europe, *Dendrochronologia*, *32*(2), 153–161, doi:10.1016/j.dendro.2014.01.002.

Baldocchi, D. (2003), Assessing the eddy covariance technique for evaluating carbon dioxide exchange rates of ecosystems: past, present and future, *Glob. Chang. Biol.*, (9), 479–492.

Baldocchi, D. (2008), "Breathing" of the terrestrial biosphere: lessons learned from a global network of carbon dioxide flux measurement systems, *Aust. J. Bot.*, *56*(1), 1–26, doi:10.1071/BT07151.

Baldocchi, D. (2014), Measuring fluxes of trace gases and energy between ecosystems and the atmosphere - the state and future of the eddy covariance method, *Glob. Chang. Biol.*, *20*, 3600–3609, doi:10.1111/gcb.12649.

Ballantyne, A. et al. (2017), Accelerating net terrestrial carbon uptake during the warming hiatus due to reduced respiration, *Nat. Clim. Chang.*, *7*, doi:10.1038/nclimate3204.

Bolton, D. (1980), The Computation of Equivalent Potential Temperature, *Mon. Weather Rev.*, *108*(7), 1046–1053, doi:10.1175/1520-0493(1980)108<1046:TCOEPT>2.0.CO;2.

Bowman, D. M. J. S., R. J. W. Brienen, E. Gloor, O. L. Phillips, and L. D. Prior (2013), Detecting trends in tree growth: Not so simple, *Trends Plant Sci.*, *18*(1), 11–17, doi:10.1016/j.tplants.2012.08.005.

Bunn, A. G. (2008), A dendrochronology program library in R (dplR), *Dendrochronologia*, *26*(2), 115–124, doi:10.1016/j.dendro.2008.01.002.

Bunn, A. G. (2010), Statistical and visual crossdating in R using the dplR library, *Dendrochronologia*, *28*(4), 251–258, doi:10.1016/j.dendro.2009.12.001.

Buttlar, J. V., J. Zscheischler, and M. D. Mahecha (2014), An extended approach for spatiotemporal gapfilling: Dealing with large and systematic gaps in geoscientific datasets, *Nonlinear Process. Geophys.*, *21*(1), 203–215, doi:10.5194/npg-21-203-2014.

Chapin, F. S. et al. (2006), Reconciling Carbon-cycle Concepts, Terminology, and Methods, *Ecosystems*, *9*(7), 1041–1050, doi:10.1007/s10021-005-0105-7.

Compo, G. P., J. S. Whitaker, and P. D. Sardeshmukh (2006), Feasibility of a 100-year reanalysis using only surface pressure data, *Bull. Am. Meteorol. Soc.*, *87*(2), 175–190, doi:10.1175/BAMS-87-2-175.

Compo, G. P. et al. (2011), The Twentieth Century Reanalysis Project, *Q. J. R. Meteorol. Soc.*, *137*(654), 1–28, doi:10.1002/qj.776.

Dee, D. P. et al. (2011), The ERA-Interim reanalysis: Configuration and performance of the data

assimilation system, *Q. J. R. Meteorol. Soc.*, *137*(656), 553–597, doi:10.1002/qj.828.

Esper, J., and D. Frank (2009), Divergence pitfalls in tree-ring research, *Clim. Change*, *94*(3–4), 261–266, doi:10.1007/s10584-009-9594-2.

Fatichi, S., S. Leuzinger, and C. Körner (2014), Moving beyond photosynthesis: from carbon source to sink-driven vegetation modeling, *New Phytol.*, *201*(4), 1086–1095.

Fritts, H. C. (1976), *Tree Rings and Climate*, Academic Press.

Harris, I., P. D. Jones, T. J. Osborn, and D. H. Lister (2014), Updated high-resolution grids of monthly climatic observations - the CRU TS3.10 Dataset, *Int. J. Climatol.*, *34*(3), 623–642, doi:10.1002/joc.3711.

Kalnay, E. et al. (1996), The NCEP/NCAR 40-year reanalysis project, *Bull. Am. Meteorol. Soc.*, *77*(3), 437–471, doi:10.1175/1520-0477(1996)077<0437:TNYRP>2.0.CO;2.

Kanamitsu, M., W. Ebisuzaki, J. Woollen, S. K. Yang, J. J. Hnilo, M. Fiorino, and G. L. Potter (2002), NCEP-DOE AMIP-II reanalysis (R-2), *Bull. Am. Meteorol. Soc.*, *83*(11), 1631–1643+1559, doi:10.1175/BAMS-83-11-1631.

Kemp, M. U., E. Emiel van Loon, J. Shamoun-Baranes, and W. Bouten (2012), RNCEP: Global weather and climate data at your fingertips, *Methods Ecol. Evol.*, *3*(1), 65–70, doi:10.1111/j.2041-210X.2011.00138.x.

Kondrashov, D., and M. Ghil (2006), Spatio-temporal filling of missing points in geophysical data sets, *Nonlinear Process. Geophys.*, *13*, 151–159, doi:10.5194/npg-14-3-2007.

Körner, C. (2015), Paradigm shift in plant growth control, *Curr. Opin. Plant Biol.*, *25*, 107–114, doi:10.1016/j.pbi.2015.05.003.

Markonis, Y., and D. Koutsoyiannis (2012), Climatic Variability Over Time Scales Spanning Nine Orders of Magnitude: Connecting Milankovitch Cycles with Hurst-Kolmogorov Dynamics, *Surv. Geophys.*, doi:10.1007/s10712-012-9208-9.

Mencuccini, M., J. Martinez-Vilalta, D. Vanderklein, H. A. Hamid, E. Korakaki, S. Lee, and B. Michiels (2005), Size-mediated ageing reduces vigour in trees, *Ecol. Lett.*, *8*(11), 1183–1190, doi:10.1111/j.1461-0248.2005.00819.x.

Mitchell, T. D., T. R. Carter, P. D. Jones, and M. Hulme (2004), *A comprehensive set of high-resolution grids of monthly climate for Europe and the globe: the observed record (1901-2000) and 16 scenarios (2001-2100)*.

Moffat, A. M. et al. (2007), Comprehensive comparison of gap-filling techniques for eddy covariance net carbon fluxes, *Agric. For. Meteorol.*, *147*(3–4), 209–232, doi:10.1016/j.agrformet.2007.08.011.

Oleson, K. et al. (2013), *Technical Description of version 4.5 of the Community Land Model (CLM)*.

Pappas, C., S. Fatichi, S. Leuzinger, A. Wolf, and P. Burlando (2013), Sensitivity analysis of a process-based ecosystem model: Pinpointing parameterization and structural issues, *J. Geophys. Res. Biogeosciences*, *118*(2), 505–528, doi:10.1002/jgrg.20035.

Peters, R. L., P. Groenendijk, M. Vlam, and P. a. Zuidema (2015), Detecting long-term growth trends using tree rings: a critical evaluation of methods, *Glob. Chang. Biol.*, *21*, 2040–2054, doi:10.1111/gcb.12826.

Piao, S. et al. (2013), Evaluation of terrestrial carbon cycle models for their response to climate variability and to CO_2 trends, *Glob. Chang. Biol.*, *19*(7), 2117–32, doi:10.1111/gcb.12187.

Pinty, B., I. Andredakis, M. Clerici, T. Kaminski, M. Taberner, M. M. Verstraete, N. Gobron, S. Plummer, and J. L. Widlowski (2011), Exploiting the MODIS albedos with the Two-Stream Inversion Package (JRC-TIP): 1. Effective leaf area index, vegetation, and soil properties, *J. Geophys. Res. Atmos.*, *116*, 1–20, doi:10.1029/2010JD015372.

Le Quéré, C. et al. (2013), The global carbon budget 1959-2011, *Earth Syst. Sci. Data*, *5*(1), 165–185, doi:10.5194/essd-5-165-2013.

Reichstein, M. et al. (2005), On the separation of net ecosystem exchange into assimilation and ecosystem respiration: Review and improved algorithm, *Glob. Chang. Biol.*, *11*(9), 1424–1439, doi:10.1111/j.1365-2486.2005.001002.x.

Sala, A., D. R. Woodruff, and F. C. Meinzer (2012), Carbon dynamics in trees: feast or famine?, *Tree Physiol.*, *32*(6), 764–75, doi:10.1093/treephys/tpr143.

Sitch, S. et al. (2003), Evaluation of ecosystem dynamics, plant geography and terrestrial carbon cycling in the LPJ dynamic global vegetation model, *Glob. Chang. Biol.*, *9*(2), 161–185, doi:10.1046/j.1365-2486.2003.00569.x.

Sitch, S. et al. (2015), Recent trends and drivers of regional sources and sinks of carbon dioxide, *Biogeosciences*, *12*(3), 653–679, doi:10.5194/bg-12-653-2015.

Wehr, R., J. W. Munger, J. B. McManus, D. D. Nelson, M. S. Zahniser, E. A. Davidson, S. C. Wofsy, and S. R. Saleska (2016), Seasonality of temperate forest photosynthesis and daytime respiration, *Nature*, *534*(7609), 680–683, doi:10.1038/nature17966.

Whitaker, J. S., G. P. Compo, X. Wei, and T. M. Hamill (2004), Reanalysis before radiosondes using ensemble data assimilation, *Mon. Weather Rev.*, *132*, 1190–1200, doi:10.1175/1520-0493(2004)132<1190:RWRUED>2.0.CO;2.

Zhu, Z., J. Bi, Y. Pan, S. Ganguly, A. Anav, L. Xu, A. Samanta, S. Piao, R. Nemani, and R. Myneni (2013), Global Data Sets of Vegetation Leaf Area Index (LAI)3g and Fraction of Photosynthetically Active Radiation (FPAR)3g Derived from Global Inventory Modeling and Mapping Studies (GIMMS) Normalized Difference Vegetation Index (NDVI3g) for the Period 1981 to 2, *Remote Sens.*, *5*(2), 927–948, doi:10.3390/rs5020927.